

Article

Effects of Metal–Support Interaction in the Electrocatalysis of the Hydrogen Evolution Reaction of the Metal-Decorated Titanium Dioxide Supported Carbon

Felipe Berto Ometto ^{1,*}, Valdecir Antonio Paganin ¹, Peter Hammer ²  and Edson Antonio Ticianelli ¹

¹ Institute of Chemistry, São Paulo University (USP), Av. Trabalhador São Carlense, 400, São Carlos 13566-590, Brazil

² Institute of Chemistry, São Paulo State University (UNESP), Rua Prof. Francisco Degni, 55, Araraquara 14800-060, Brazil

* Correspondence: felipebertoometto@yahoo.com.br

Abstract: It has been found that the electrocatalytic properties of metallic nanoparticles supported on transition metal oxides are affected by the existing strong metal–support interaction (SMSI). Herein, the effects of SMSI on the electrocatalysis of the hydrogen evolution reaction (HER) were investigated in acid electrolyte by using Pt and Ag nanoparticles supported on carbon and titanium oxide (TiO₂). High-resolution transmission electron microscopy (HR-TEM) images showed that Pt and Ag nanoparticles present a spherical shape at the TiO₂ support and an average size distribution of around 4.5 nm. The X-ray photoelectron spectroscopy (XPS) results for Pt/TiO₂/C and Ag/TiO₂/C evidenced higher amounts of surface oxides in the metallic particles, when compared to the materials supported on carbon. Consistently, electrode polarization and electrochemical impedance results revealed that both metal–TiO₂ and metal–C-supported catalysts were more active in catalyzing the HER than the corresponding carbon-supported materials, with Pt presenting better results. These differences in the HER activities were related to the electronic effects of the TiO₂/C substrate on the Pt and Ag metals, introduced by strong metal-support (SMSI) in the metal–TiO₂/C catalysts.

Keywords: hydrogen evolution reaction; decoration effects; support effects; charge transfer; activity-property correlations



Citation: Ometto, F.B.; Paganin, V.A.; Hammer, P.; Ticianelli, E.A. Effects of Metal–Support Interaction in the Electrocatalysis of the Hydrogen Evolution Reaction of the Metal-Decorated Titanium Dioxide Supported Carbon. *Catalysts* **2023**, *13*, 22. <https://doi.org/10.3390/catal13010022>

Academic Editors: Francesco Enrichi, Alberto Vomiero and Elti Cattaruzza

Received: 17 November 2022

Revised: 14 December 2022

Accepted: 20 December 2022

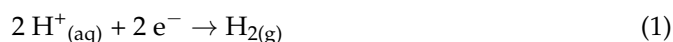
Published: 23 December 2022



Copyright: © 2022 by the authors. Licensee MDPI, Basel, Switzerland. This article is an open access article distributed under the terms and conditions of the Creative Commons Attribution (CC BY) license (<https://creativecommons.org/licenses/by/4.0/>).

1. Introduction

As a result of global warming and atmospheric air pollution, a reduction in the utilization of oil derivatives for energy conversion has become a decisive factor if there is to be sustainable global development. In this regard, research into energy conversion without the release of pollutants has been directed towards the use of green hydrogen as fuel, particularly that produced electrochemically at the cathode of a water electrolyzer, where the hydrogen evolution reaction (HER) takes place. In this process, hydrogen molecules are produced by the reduction of protons in an acidic media and water molecules in alkaline media [1], as given by:



Noble metals-based materials promote HER with the smallest activation energies, with platinum being the most active metal in acid solutions. However, the high cost and scarcity of this metal has driven much research into the development of non-noble metal catalyst composites and/or of catalysts with ultra-low loading of the noble metals. Since the electrocatalytic process occurs at active sites located on the surfaces of the catalyst particles, reducing the size of such particles, or the use of single atoms and clusters, are strategies that have been widely explored to enhance the efficiency of materials utilization. Platinum

single atoms dispersed on carbon-based compounds [2–6], such as N-doped graphene, can provide high HER activity, by promoting a lowering of the Pt 5d band occupancy [7]. This allows its interaction with the 1s orbital of H atoms, that facilitates formation of the H₂ molecules. In addition, theoretical calculations have shown that the electron exchange of Pt atoms on the surface of a Pt₄₄ cluster with a carbon composite substrate is less effective than that of an isolated single Pt atom. This indicates that after the H adsorption, the Pt atoms on the cluster remain metallic, while the isolated single Pt atoms become non-metallic, due to electron donation, either to the substrate or to the H atoms [7].

Improved activity in hydrogen evolution [8–16], oxygen reduction [17–23], hydrogen oxidation and CO oxidation [24–26] reactions were also reported for Pt, Ni, Fe, Au, Co nanoparticles supported on oxides, carbides and other materials. For Pt nanoparticles supported on transition metal oxides, experimental results indicated changes of the electrochemical activity promoted by electron transfer between the support and the metal nanoparticle. This process, known as strong metal–support interaction (SMSI) [27], results in changes in the occupancy of the metal valence band [28] and, consequently, in the density of Pt 5d states near the Fermi level that become different from that of bulk metallic Pt [29,30]. This electron transfer can be strong enough to promote compressive strain [31] and alloy formation [32], which can lead to an increase in the catalytic activity.

In electrocatalysis, it is well established that the activity of metals to promote a reaction is related to their electronic structure. Thus, changes in this property by SMSI can modify the binding energy of adsorbates on the metal particle surface, changing its catalytic activity for a given reaction. In this way, the use of SMSI to modify the electronic structure of metals that are less noble, such as silver, may be an excellent strategy for the manufacturing of electrocatalysts with improved activity for the HER. However, high filling of the antibonding d orbitals makes the number of antibonding H(1s)–(d)M bonds low, so that the adsorption energy of hydrogen on the surface is low, making the catalytic activity moderate [33]. Thus, changing Ag's electronic structure through the use of SMSI could increase the electrocatalytic performance for HER.

In this work, we report on an investigation of the activity of low loading Pt and Ag nanoparticles anchored on a titanium oxide/carbon substrate prepared by a microemulsion method, as electrocatalysts for the hydrogen evolution reaction in acid media. The effects of metal–support interactions, elucidated using different techniques, on the electrolytic activity are discussed for the distinct materials.

2. Results and Discussion

2.1. Catalyst Properties

XRD diffractograms for the 1% Pt/TiO₂/C and 1% Ag/TiO₂/C catalysts in Figure 1 only showed peaks related to TiO₂ anatase (JCPDS 73-1764) and rutile (JCPDS 73-1765) phases. No signals related to the presence of metallic structures were observed, as expected, considering the small contents of platinum and silver. As shown in Figure S1 from Supplementary Materials, no signal characteristic of the titanium carbide at 36°, 41.9°, 60.7°, 72.6° and 76.4° (JCPDS 65-8807) was observed. In the case of the 1% M/C catalysts (Supplementary Materials Figure S2), the characteristic signal of the amorphous carbon support was seen at 2θ around 25°. Only the XRD of 1% Ag/C evidenced the presence of metallic structures, possibly due to the presence of enlarged particles, formed by the sintering of silver ultra-nanoparticles, occurring along the heating-treatment involved in the synthesis.

High resolution XPS spectra of the Pt 4f and Ag 3d orbitals are presented in Figure 2. Compositions of the surface layer of catalyst particles are shown in Table 1. Figure 2 shows the fitted lines of the Pt 4f spectra of the 1% Pt/C and 1% Pt/TiO₂/C for components corresponding to Pt⁰ and two oxidized states (Pt²⁺ and Pt⁴⁺), referred to as Pt(OH)₂ and PtO₂ [34] species, respectively. The Ag 3d spectra of the 1% Ag/C and 1% Ag/TiO₂/C could be appropriately fitted for the metallic component Ag⁰ and the oxidized states AgO_x [35,36]. The binding energies and atomic percentages of the Pt⁰, Pt^{δ+}, Ag⁰ and Ag^{δ+}

species are shown in Table 1. The binding energies of the Pt^0 and Ag^0 species are the same for samples supported on TiO_2/C or on carbon alone. These results were in agreement with those reported for Pt particles in C-MOx supports [28,37], but differed from those reported for Pt/ TiO_2/C and Pt/ WO_3/C [38,39] and those published for Pt/ TiO_2 and Pt/M- TiO_2 (M = V, Cr and Nb) [40], where a decrease in the binding energies was observed, compared to Pt/C. These differences in the binding energies could be attributed to differences in the metal morphology, lattice parameters, loads, particle sizes, and the distribution of metallic nanoparticles on the support.

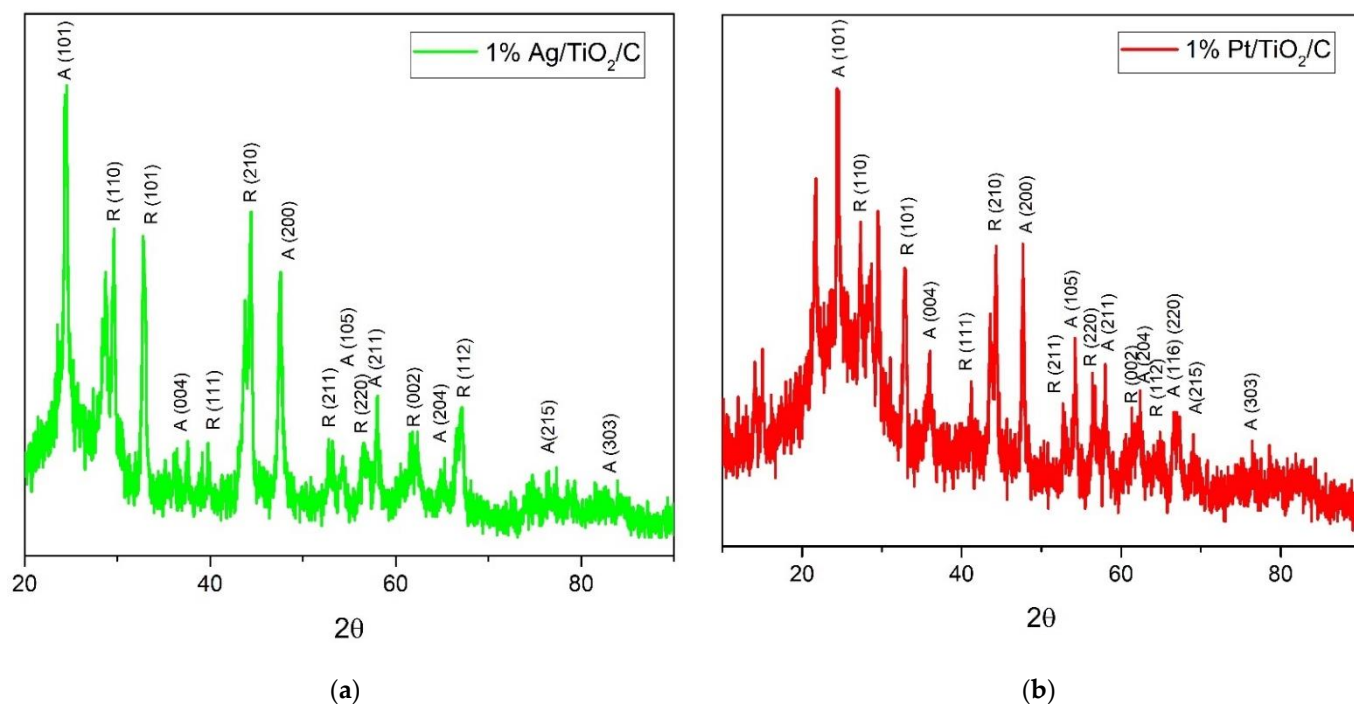


Figure 1. XDR of 1% Ag/ TiO_2/C (a) and 1% Pt/ TiO_2/C (b). The titanium phases are indicated by A (anatase) and R (rutile).

The results in Table 2 show that the amounts of oxidized species ($Pt^{\delta+}$ and $Ag^{\delta+}$) in the materials supported on TiO_2/C were greater than those supported on carbon. This might be related to the electronic sharing induced by the metal–support interaction that would remove electronic density of the metal, making its surface more oxidized. As shown in the supplementary material (Supplementary Materials Figure S3), only the signal referring to the Ti^{4+} component was observed in the Ti 2p spectrum. The results showed that the binding energy of Ti 2p was similar, independent of the material.

These results denoted that the concentrations of platinum and silver were below the nominal values, particularly in the case of silver. This deviation might arise in the filtration steps involved in the synthesis of the catalyst, where loose metallic particles might be leached out. On the other hand, it should be mentioned that the concentrations were calculated from the metal content on the surface of the particles, where they were predominantly in the oxide form of metal oxides, especially in the case of Ag. In this way, the obtained value might not represent the global content of the element. An important aspect to be noted here is that in both cases, the Ag and Pt loads were the same in the carbon and TiO_2/C substrates (Table 1), a favorable condition in which to discuss the SMSI interaction.

The images of HR-TEM showed that in the 1% Pt/ TiO_2/C and 1% Ag/ TiO_2/C materials (Figure 3) there were large prismatic and spherical particles of titanium oxide with sizes between 20 to 200 nm. Some of the spherical particles could be related to Vulcan carbon that is known to be sized around 20 nm. Regarding TiO_2 , the presence of mixed morphologies might be explained by considering the possibility of the formation of one kind of particle outside the micelle (prismatic) and the other inside the micelle (spherical) within the microemulsion method

of preparation of the materials. It was also observed that Pt and Ag were uniformly dispersed as nanoparticles deposited on titanium oxide and on carbon. These metallic nanoparticles presented a spherical shape with average sizes of 4.5 ± 0.1 nm and 4.3 ± 0.1 nm in the 1% Ag/TiO₂/C and 1% Pt/TiO₂/C catalysts, respectively, as shown in the histograms of Figure 4. Although the presence of nanoparticles could be observed in the images obtained for the carbon-supported catalysts 1% Ag/C and 1% Pt/C (Supplementary Materials Figure S4), platinum and silver were predominantly present in the form of ultra-small aggregates, the sizes (<1 nm) of which could not be determined, due to insufficient resolution of the microscope used in these studies.

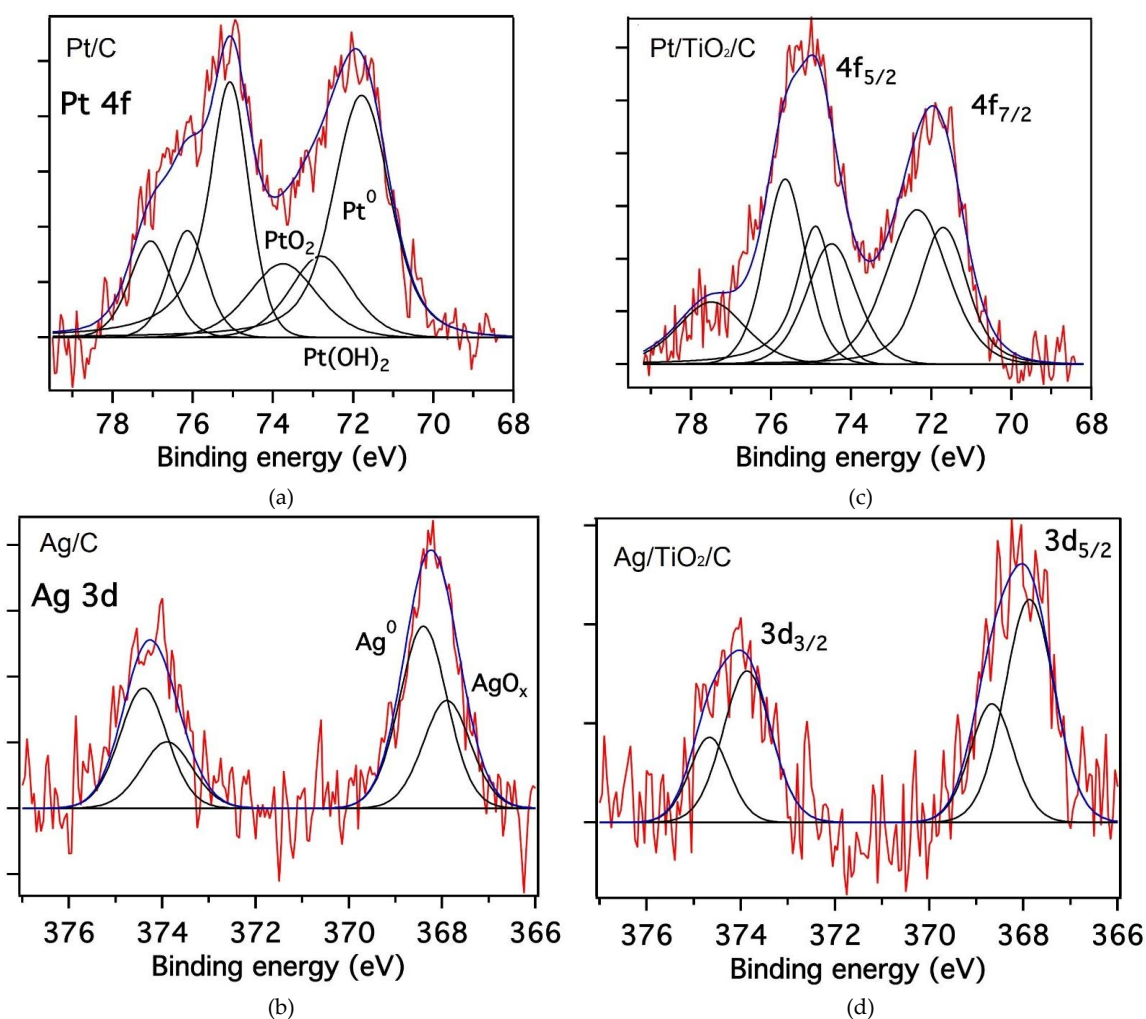


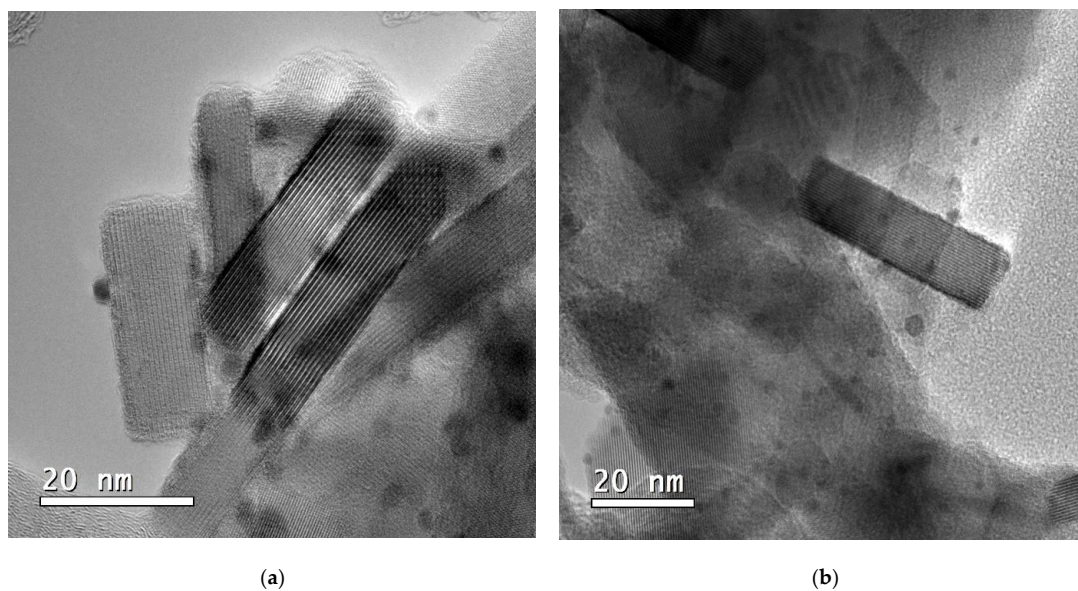
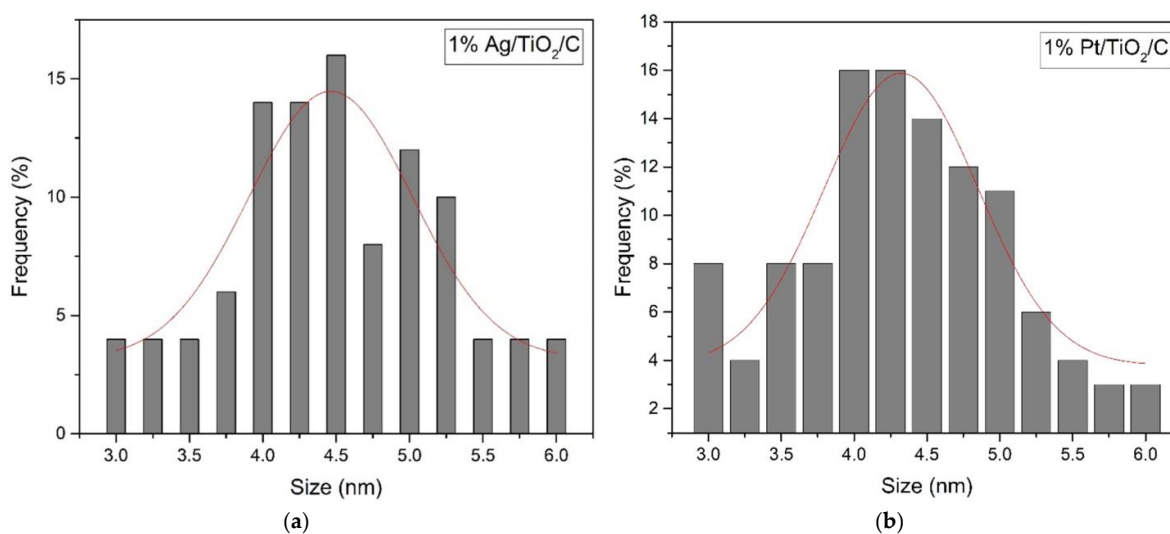
Figure 2. Deconvoluted Pt 4f and Ag 3d XPS spectra for (a) 1% Pt/C, (b) 1% Ag/C, (c) 1% Pt/TiO₂/C, and (d) 1% Ag/TiO₂/C catalysts.

Table 1. Surface composition of catalysts obtained by XPS.

Elements	Composition (wt.%)				
	Pt/C	Ag/C	Pt/TiO ₂ /C	Ag/TiO ₂ /C	TiO ₂ /C
Oxygen (O 1s)	7.9	6.2	15.4	16.8	19.8
Carbon (C 1s)	91.3	93.6	80	75.8	73.7
Platinum (Pt 4f)	0.7	-	0.7	-	-
Silver (Ag 3d)	-	0.3	-	0.3	-
Titanium (Ti 2p)	-	-	3.9	7.2	6.5

Table 2. Results obtained from XPS analyses.

Catalyst	Pt 4f _{7/2} —Binding Energy/eV	Species	% (atomic)
1% Pt/C	71.7	Pt ⁰	60
	72.8	Pt ^{d+}	40
	73.7		
1% Pt/TiO ₂ /C	71.7	Pt ⁰	33
	72.5	Pt ^{d+}	67
	74.3		
Catalyst	Ag 3d _{5/2} —Binding Energy/eV	Species	% (atomic)
1% Ag /C	368.4	Ag ⁰	63
	367.9	Ag ^{d+}	37
1% Ag/TiO ₂ /C	368.6	Ag ⁰	32
	367.9	Ag ^{d+}	69

**Figure 3.** HR-TEM images obtained for 1% Ag/TiO₂/C (a) and 1% Pt/TiO₂/C (b).**Figure 4.** Particle size for 1% Ag/TiO₂/C (a) and 1% Pt/TiO₂/C (b).

2.2. Hydrogen Evolution in Acid Medium

The CV curves obtained in H_2SO_4 solution for all catalysts are shown in Supplementary Materials Figure S5. As expected from the previous results, in the hydrogen adsorption/desorption processes close to 0.4 V, characteristics of polycrystalline materials, were not observed, due to the low presence of Pt and Ag in the materials. Furthermore, the CV responses matched those normally found for capacitive interfaces, involving very similar current densities for all catalysts, being consistent with similar overall electrochemical surface areas (active centers and support).

A typical set of ohmic drop-corrected HER polarization curves (current density (j) vs. electrode potential, $j =$ current per unit geometric area, usually taken as the electrode activity) for 1% M/ TiO_2 /C and 1% M/C catalysts is shown in Figure 5a, along with those obtained by re-plotting the data, but with the current divided by the catalyst mass in the electrode (j_m), Figure 5b. Here the masses corresponded to those of TiO_2 /C for the substrate and the metals in the other cases, j_m usually being taken as the mass activity of the catalyst. Taking the result for TiO_2 /C as a reference, a decrease in the reaction overpotentials was clearly observed, as seen in Figure 5a, when comparing the polarization curves of all other catalysts. Considering these results (Figure 5a), the following trend could be found regarding the electrode activities: TiO_2 /C < 1% Ag/C < 1% Ag/ TiO_2 /C < 1% Pt/C < 1% Pt/ TiO_2 /C < 20 %Pt/C.

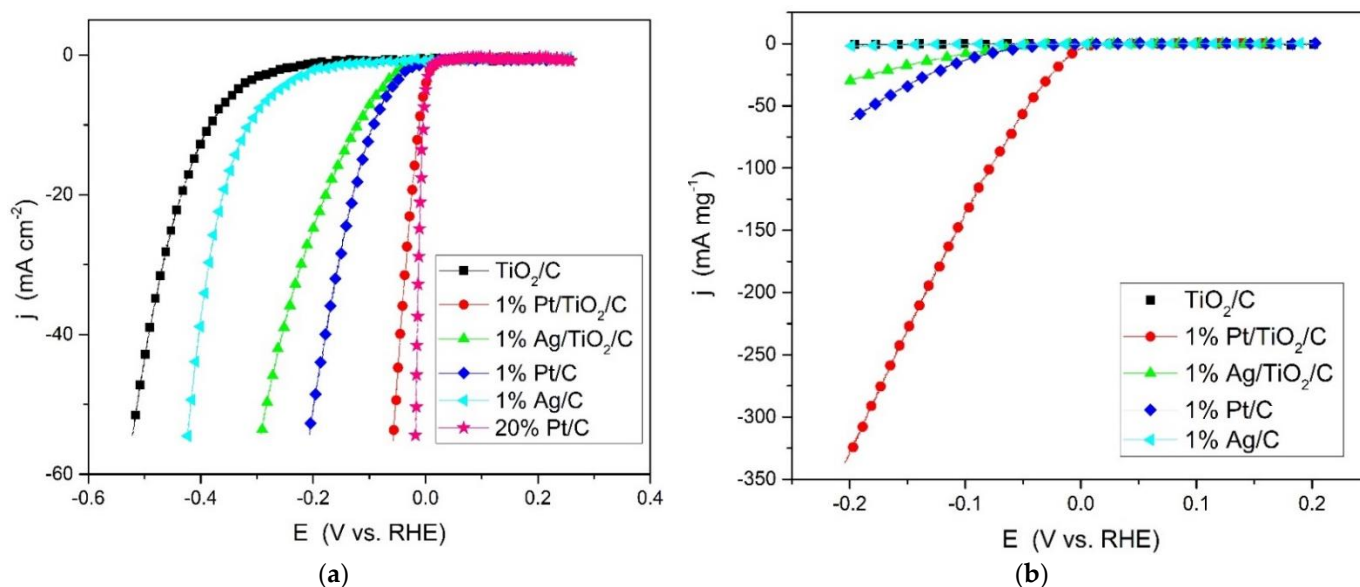
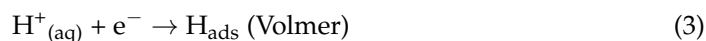


Figure 5. IR-corrected RHE polarization curves measured at the disk electrode in Ar-saturated 0.5 M H_2SO_4 solution (a) and normalized by catalyst mass (b). Scan rate: 5 mV s^{-1} . Rotation rate: 3600 rpm.

On the other hand, the results in Figure 5b show that, among all prepared catalysts, 1%Pt/ TiO_2 /C presented the highest mass activity. These results also denoted that the HER mass activity considerably improved with anchoring of the metallic active centers (Pt and Ag) in the TiO_2 /C substrate, instead of carbon, with Pt presenting better results as compared to Ag. Changes in the mass activity of a given catalyst are usually assigned to two factors: changes on the specific surface area or changes on the electronic properties, caused, for example, by SMSI. In the present cases, as discussed above, the Ag and Pt particles were predominantly in the form of ultra-small aggregates when anchored in carbon and in the form of nanoparticles when anchored in TiO_2 /C, meaning that the specific active surface areas were smaller in the M/ TiO_2 /C catalysts. Since the corresponding metal loads were the same on M/C and M/ TiO_2 /C (Table 1), one might conclude that the differences in the HER activities were mainly related to electronic effects. This fact clearly evidenced that SMSI effects presented in the M/ TiO_2 /C catalysts were very efficient in increasing the catalytic activity of the metal centers.

2.3. The Reaction Mechanism

There is a consensus that in an acidic environment the HER takes place in two stages with two possible mechanisms [41,42]. The process starts with electrochemical hydrogen adsorption on the surface of the catalyst, called the Volmer reaction (3), where one electron is transferred to form an intermediate adsorbed hydrogen atom [43].



The subsequent step, involves formation of the hydrogen molecules through two alternative routes; the adsorbed species can react with a proton from the electrolyte in a process known as the Heyrovsky reaction [44] or it can combine with other H_{ads} present on the catalyst surface to generate H_2 via the Tafel reaction [45].



For a given catalyst, the actual HER mechanism can be analyzed in terms of the values of the so-called Tafel slope, that corresponds to the slope of potential vs. logarithm of current density profiles. These values can be deduced by theoretical kinetic analysis of the HER in acid media, in the following terms [46,47]: (i) when the Heyrovsky and Tafel reactions are much faster than the Volmer step, theoretical calculations would predict a Tafel slope of 0.12 V dec^{-1} at 25°C ; (ii) when the mechanism is assumed to be formed only by the Volmer/Heyrovsky reactions, with the Heyrovsky being the rate determining step (rds), the theoretical Tafel slope would result in 0.39 V dec^{-1} ; (iii) finally, when the mechanism is formed by the Volmer/Tafel steps, having the Tafel reaction as rds, the theoretical slope results in 0.29 V dec^{-1} .

Here, the IR-correct potentials were used to construct the Tafel lines (E vs. log j) shown in Figure 6, for the acid electrolyte, the corresponding slopes (Tafel slopes) of which are shown in the figure. According to the Tafel slope values, the catalysts could be divided into three categories: TiO_2/C and 1% Ag/C promoted HER with Tafel slope values in the range of 0.16 V dec^{-1} ; 1% $\text{Ag}/\text{TiO}_2/\text{C}$ promoted the reaction with Tafel slope values between 0.06 V dec^{-1} ; and 1% Pt/C , 1% $\text{Pt}/\text{TiO}_2/\text{C}$ and 20% Pt/C presented Tafel slopes close to 0.03 V dec^{-1} . These values of the Tafel slopes suggested that the rate-determining step for the HER on the TiO_2/C and 1% Ag/C catalysts (0.16 V dec^{-1}) would be the Volmer reaction, followed by the faster Heyrovsky and/or Tafel steps. For the 1% $\text{Ag}/\text{TiO}_2/\text{C}$ (0.06 V dec^{-1}), the rate-determining step of the HER would be the Heyrovsky reaction, with the Volmer step occurring rapidly and no appreciable participation of the Tafel step. For the 1% Pt/C , 1% $\text{Pt}/\text{TiO}_2/\text{C}$ and 20% Pt/C materials (0.03 V dec^{-1}), the rate-determining step was the Tafel step, and the mechanism comprised the Volmer and Tafel steps, with negligible involvement of the Heyrovsky reaction.

Further insights on the reaction mechanism were obtained from the electrochemical impedance results. Figure 7 shows a comparison of the electrochemical Nyquist impedance plots obtained for the HER promoted by the different catalysts at -0.2 V vs. RHE . The results showed that the impedance profiles were apparently dominated by a single arc, the magnitude of which was related to the polarization resistance of the HER rate determining step that determined the polarization responses of the different catalysts. Analyses of these results were made using an electric equivalent circuit (EEC) model, proposed by Armstrong and Henderson [48] (Supplementary Materials Figure S6). In this model R_s is the solution resistance, in series with the interface circuit. CPE, R_1 , CP, R_2 reflect the response of a HER system characterized by two-time constants, the first one, $\tau_1(\text{CPE}-R_1)$, related to the charge transfer kinetics (Heyrovsky step) and the second one, $\tau_2(\text{CP}-R_2)$, related to hydrogen electrochemical adsorption [49–51] (Volmer step). Fitting software (Zview) was used to adjust the parameters until the simulated data were the most adequate to represent the experimental phenomena occurring at the electrode interface. Examples of the theoretical

line adjusted to the experimental results are shown in Supplementary Materials Figure S7. In general, fit to the Armstrong circuit was good for the systems discussed here and the resulting values fitting parameters are summarized in Table 3. In this Table, the faradaic resistance R_F corresponds to the sum of R_1 and R_2 resistances.

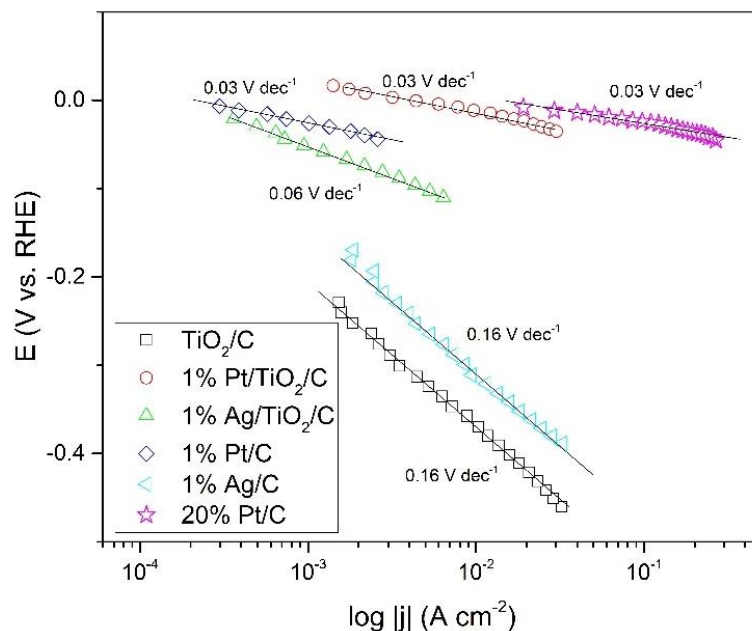


Figure 6. Comparison of Tafel plots for TiO_2/C , 1% Pt/ TiO_2/C , 1% Ag/ TiO_2/C , 1% Pt/C, 1% Ag/C and 20% Pt/C catalysts. The slope of the lines corresponds to 0.16 V dec $^{-1}$, 0.03 V dec $^{-1}$, 0.06 V dec $^{-1}$, 0.03 V dec $^{-1}$, 0.16 V dec $^{-1}$ and 0.03 V dec $^{-1}$, respectively.

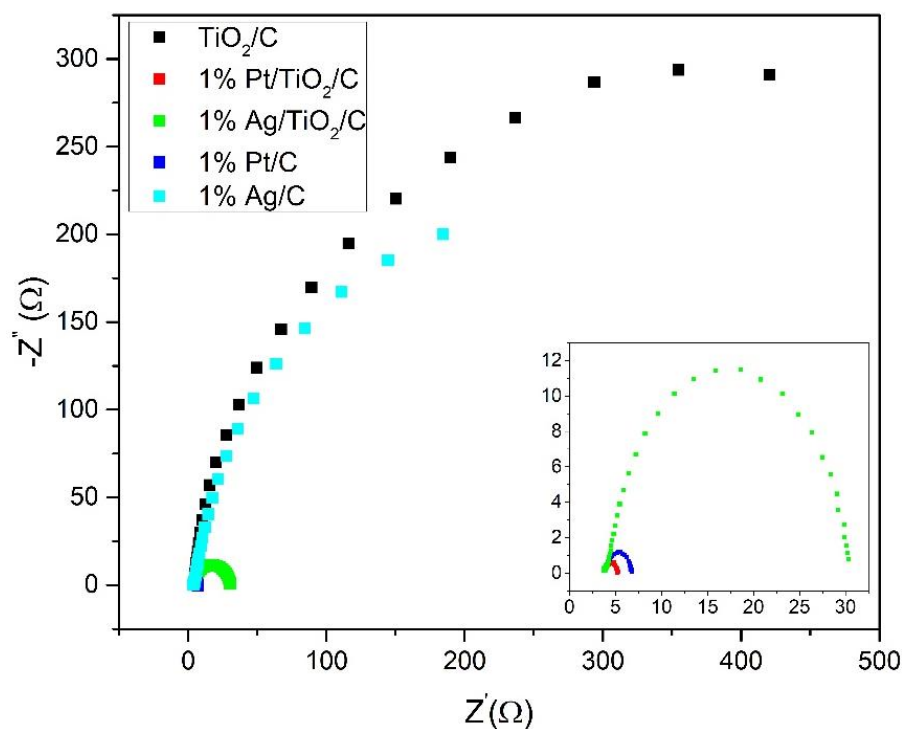


Figure 7. Electrochemical impedance measured in Ar-saturated 0.5 M H_2SO_4 solution for M/ TiO_2/C and M/C catalysts. $E = -0.2$ V vs. RHE, rotation rate: 3600 rpm.

Table 3. Electric equivalent circuit parameters of catalysts where CPE-T is related to capacitance and CPE-P to irregularity of the analyzed surface tending to 1 for perfectly flat surfaces. The faradaic resistance R_F corresponds to the sum of resistors R_1 and R_2 .

Material	CPE-T	CPE-P	C_P	R_1 (Ω)	R_2 (Ω)	R_F (Ω)
TiO ₂ /C	0.0012	0.90	0.0005	3	4042	4045
1% Ag/TiO ₂ /C	0.0022	0.84	0.0013	1.6	25	26.6
1% Pt/TiO ₂ /C	0.0016	0.78	0.0004	0.6	0.9	1.5
1% Ag/C	0.0034	0.85	0.0010	5.1	506	511
1% Pt/C	0.0024	0.74	0.0006	0.5	2.6	3.1

From the results in Table 3, it is observed that addition of transition metals to the TiO₂/C substrate, instead of carbon, promoted a decrease in the R_F , resulting specifically from a reduction of R_2 . This effect might come from a more effective electron transfer from the TiO₂/C to the metallic clusters, that allowed the electrochemical hydrogen adsorption to occur faster or more strongly. Faster hydrogen adsorption could alter the rate-determining step of the HER reaction in materials for which, in the absence of a metal-substrate interaction, the Volmer step limited the rate of the process, causing a change in the observed Tafel coefficient. In this way, the high R_2 resistance observed for TiO₂/C and Ag/C would imply a slow hydrogen electrochemical adsorption, making the Volmer reaction the rate-determining step, as observed by Tafel diagrams (slope 0.16 V dec⁻¹). However, when Ag was supported on TiO₂, values of R_2 decreased drastically, evidencing a faster hydrogen adsorption and, therefore, an increase in the rate of the Volmer reaction that made the Heyrovsky reaction the rate-determining step, as confirmed by the Tafel coefficient (0.06 V dec⁻¹) obtained in these cases. Finally, for the Pt-containing materials (1% Pt/C and 1% Pt/TiO₂/C), low R_2 resistance values were observed, as seen in Table 3, in all cases, implying that the Volmer step was quite fast. Interactions with TiO₂ could modulate the magnitude of the Pt-H_{ads} bond strength, optimizing it, and resulting in an increase of the rate of Tafel reaction, that now became the rate-determining step, as evidenced by the Tafel slopes of 0.03 V dec⁻¹ in all cases.

2.4. Electronic Effects in HER

In the systems presented, the SMSI effect could be discussed in terms of the overlap of the d bands of Ti with those of Pt and Ag, that might promote an increase in the energy of the Pt and Ag anti-ligand orbitals, causing an electron transfer from the metal to the TiO₂ support, increasing the Pt and Ag oxidation states. In the case of Pt, the emptying of the 5d band by SMSI was confirmed by Villullas et al. [28,37], for similar Pt nanoparticles supported on TiO₂/C. Likewise, the effect was also reported for single Pt atoms, for which the electron removal originated from coordination with C-N centers in nitrogen-doped reduced graphene oxide [4,5]. Consistently, the experimental results obtained here showed that the SMSI involved in the M/TiO₂/C catalysts led to an increase of the amount of oxidized metal on the surface of the nanoparticles.

It is well known that the adsorption of hydrogen on Pt occurs through the hybridization of the 1s orbitals of hydrogen and the 5d band of Pt, that promotes formation of ligand and anti-ligand orbitals. Since the SMSI effect leads to an increase in the number of Pt 5d states above the Fermi level, the pairing of electrons with the hydrogen atom leads to stronger M-H bonding [5]. In this sense, the increased catalytic activity observed here for Pt/TiO₂/C, which had the Tafel reaction (reaction 5) as the rate-determining step, was surely related to the increased surface coverage of adsorbed hydrogen atoms, H_{ad}. In the cases of Ag/C, the HER rate-determining step was the Volmer reaction. However, for Ag/TiO₂/C, emptier Ag 4d states above the Fermi level, resulting from the SMSI effect, the rate of the Volmer step would increase, thus, turning the Heyrovsky reaction into the rate-determining step, in agreement with what was predicted from the Tafel slopes and electrochemical impedance analyses.

2.5. Catalyst Stability

The accelerated degradation experiments were performed by cyclic voltammetry (CV), running 1010 cycles at 100 mV s^{-1} . The polarization curves obtained after the 5th. and 1010th. cycles are shown in Figure 8. These polarization results showed that, within the experimental error, the activities of the Pt/TiO₂/C and Ag/TiO₂/C materials were the same before and after 1010 cycles, confirming the excellent stability of the M/TiO₂/C materials as catalysts for the HER. In the case of Ag/TiO₂/C, although very small, there were some changes of the slope of the polarization curves, after 1010 cycles, and this was probably associated to a reduction of ohmic drop and/or some restructuring of the Ag particles surface along the cycling, that also slightly retarded the onset potential of the HER.

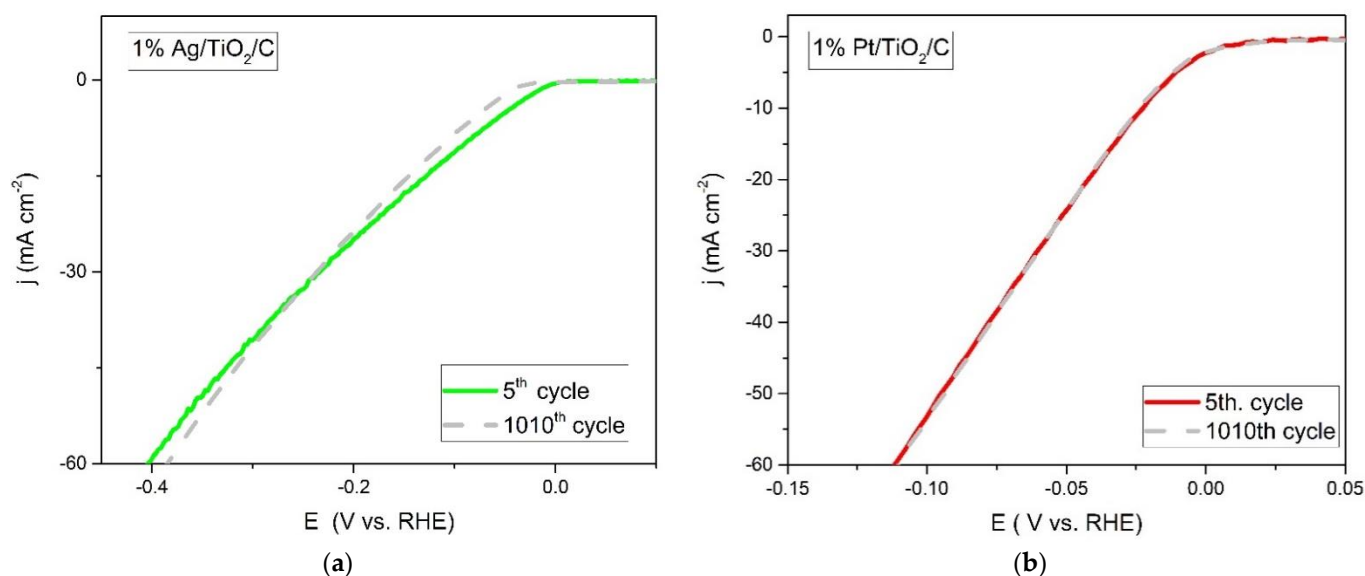


Figure 8. HER polarization curves collected before and after 1000 cycles in Ar-saturated 0.5 M H₂SO₄ solution obtained for 1% Ag/TiO₂/C (a) and 1% Pt/TiO₂/C (b). Scan rate: 5 mV s^{-1} . Rotation rate: 3600 rpm.

3. Materials and Methods

3.1. Preparation of TiO₂/C

TiO₂ nanoparticles were synthesized in heptane by the microemulsion method [52–55] with the decomposition of the metal precursor titanium isopropoxide inside of the water micelles. Briefly, 90 mL of heptane (Sigma-Aldrich, St. Louis, MO, USA, 97%), 18 g of sodium dodecyl sulfosuccinate (AOT) (Sigma-Aldrich, St. Louis, MO, USA, 97%) and 5.84 mL of ultra-pure water were mixed and kept under stirring. After 2 h, a mixture containing 0.6 mL of titanium isopropoxide in 5 mL of heptane was added to the microemulsion. The system was then stirred for 21 h to form titanium oxide. To prepare TiO₂/C this material was anchored onto 90 mg of carbon powder (Vulcan XC-72, Cabot Corporation, Boston, MA, USA) for 22 h and washed with ethanol. The collected solid was dried in air at 80 °C for 1 h. Thermal treatment of the powder was performed in CH₄/H₂ (50:50) atmosphere using a ramp of 2 °C/min from 25 °C for up to 900 °C, which was maintained for 30 min.

3.2. Preparation of M/TiO₂/C Catalysts

Titanium oxide was decorated with Pt and Ag through a microemulsion containing the metallic precursors. The metallic precursor solution contained 4.6 mg of chloroplatinic acid (H₂PtCl₆·6H₂O) or 2.83 mg of silver nitrate (AgNO₃). In the synthesis, 9 mL of heptane and 1.2 g of AOT were mixed with a 0.36 mL of metallic precursor aqueous solution. After stabilization (1 h under stirring), these solutions were drop-wise added to the previously prepared microemulsion containing titanium oxide. The system was stirred for 6 h and then 1.5 mL of tetraethyl orthosilicate was added to the mixture. The reaction was carried out for 17 h under mechanical stirring. Then the metal/TiO₂ material was anchored onto 90 mg of

carbon powder (Vulcan XC-72, Cabot Corporation, Boston, MA, USA) for 22 h. The composite was filtered and washed with ethanol and the collected solid dried in air at 80 °C for 1 h. Thermal treatment of the powder was performed in CH₄/H₂ (50:50) atmosphere using a ramp of 2 °C/min from 25 °C for up to 900 °C, which was maintained for 30 min. The material was washed and finally filtered with aqueous KOH solution and water to remove Si compounds. The Pt/TiO₂/C and Ag/TiO₂/C catalysts were prepared with 1 wt.% Pt and Ag loadings and with a titanium oxide to carbon proportion of 50:50 wt.%.

3.3. Preparation of M/C Catalysts

A microemulsion containing 9 mL of heptane, 1.2 g of AOT and 0.36 mL of aqueous solution of the metal precursors (same amounts as in the previous process) was added dropwise to a dispersion containing 180 mg of Vulcan carbon in 50 mL of heptane. After 6 h of stirring, 1.5 mL of tetraethyl orthosilicate was added to the mixture, and left to react for 17 h. The system was washed and filtered with ethanol and the collected solid, dried at 80 °C and subjected to a heating treatment at 900 °C for 30 min with a ramp of 2 °C/min in an atmosphere of H₂/N₂ (6 mol% H₂). The materials were washed and filtered with aqueous KOH solution and water. The Pt/C and Ag/C catalysts were prepared with 1 wt. % Pt and Ag.

3.4. Catalyst Characterization

X-ray diffraction analyses (XRD) were performed with an Ultima IV equipment, model Ru200B (Rigaku Corporation, Tokyo, Japan) using Cu K α radiation (1.5406 Å) and recorded at 0.5 degrees min⁻¹ for 2 θ values between 20° and 100°. The diffractograms were analyzed with the Crystallographica-Search Match 2.1 (Oxford Cryosystems Ltd., Oxford, UK).

Catalyst morphology was investigated by acquisition of images of high-resolution transmission electron microscopy using a JEM-2100 (JEOL, Tokyo, Japan) microscope operating at 200 kV. The samples were prepared by directly applying an isopropyl alcohol suspension of the catalyst powder onto standard Au TEM grids. The average particle size was evaluated by determining the size of 100 particles with the help of the ImageJ 1.5.3 (National Institutes of Health, Bethesda, MD, USA).

The XPS analysis was carried out at a pressure of less than 10⁻⁷ Pa using a commercial spectrometer (UNI-SPECS UHV Surface Analysis System, SPECS, Berlin, Germany). The Mg K α line was used ($h\nu = 1254.6$ eV) and the analyzer energy pass for the high-resolution spectra was set to 10 eV. The inelastic background of the Pt 4f and Ag 3d core level spectra was subtracted using Shirley's method. The elemental composition of the surface layer (<5 nm) was determined with an accuracy of $\pm 5\%$ from the relative proportions of the peak areas, corrected by Scofield's atomic sensitivity factors. The spectra were fitted without placing constraints with multiple Voigt profiles (70% Gaussian and 30% Lorentzian function) [56–60] using the CasaXPS 2.3 (The width at half maximum (FWHM) varied between 1.2 and 2.1 eV and the accuracy of the peak positions was ± 0.1 eV).

3.5. Electrochemical Measurements

A Bipotentiostat model AFCBP1 (Pine Research Instruments, Durham, USA) and a conventional three-compartment electrochemical cell were used for all the experiments. Counter electrodes of graphite were used in the 0.5 M H₂SO₄ electrolyte solution. The potentials were measured against a reversible hydrogen reference electrode. The electrochemical measurements were performed in argon-saturated solution. The catalysts were tested in the form of ultrathin layers, which were obtained by depositing 20 μ L of a catalyst ink on a glassy carbon disk (0.247 cm² Pine Research Instruments, Durham, NC, USA). The catalyst ink was prepared with 10 mg of catalyst powder, 1.0 mL of isopropyl alcohol and 45 μ L of Nafion[®] solution. The catalyst load (carbon + TiO₂ + metal) or (carbon + metal) on the working electrode was 0.81 mg cm⁻². Cyclic voltammetry (CV) experiments were carried out in the potential range of 0.05 to 1.0 V at a scan rate of 50 mV s⁻¹. The rotating disk electrode technique (RDE) was used to investigate the electrocatalytic activity and stability, by recording HER polarization curves in the potential range of 0.4 V to -0.6 V at a sweep rate

of 5 mV s^{-1} . The ohmic drop caused by the electrolyte resistance was obtained from the high frequency intercept of Nyquist impedance spectroscopy plots for the cells with the different materials in the 0.5 M of H_2SO_4 electrolyte and the average values were found to be $0.9 \Omega \text{ cm}^2$. Electrochemical impedance experiments were performed with a potentiostat PGSTAT 302N (Metrohm Autolab, Utrecht, The Netherlands) in the frequency range from 1000 kHz to 0.1 Hz, at polarization potentials from -0.1 to -0.6 V, using the rotating disk electrode. All electrochemical measurements were carried out at room temperature ($T = 25 \text{ }^\circ\text{C}$).

4. Conclusions

From the results discussed here it was concluded that the synthesis method resulted in a mixture of anatase and rutile phases of TiO_2 , with nanoparticle sizes between 20 to 200 nm and spherical and prismatic shapes. The decoration of this material with Pt and Ag resulted in the formation of metallic spherical nanoparticles with average sizes close to 4.5 nm. Surface atoms in the Pt and Ag particles were found to be preponderantly in the metallic state, but some oxidized elements were also present. The 1% Pt/ TiO_2 /C and 1% Ag/ TiO_2 /C materials presented a higher degree of particle surface oxidation, as compared to 1% Pt/C and 1% Ag/C, indicating that the SMSI promoted the decrease of d band occupancy of the metallic atoms.

Electrochemical results denoted that the HER mass activity considerably improved by anchoring the metallic active centers in TiO_2 /C substrate instead of carbon, with Pt exhibiting better results compared to Ag. These differences in the HER activities were mainly related to electronic effects on the Pt and Ag metals, introduced by SMSI in the M/ TiO_2 /C catalysts. From the Tafel analyses it was concluded that, for the 1% Ag/ TiO_2 /C, the HER occurred via the Volmer and Heyrovsky mechanisms, with the Heyrovsky reaction corresponding to the rate-determining step, while, for the 1% Pt/ TiO_2 /C, 1% Pt/C and 20% Pt/C materials, the HER mechanism comprised the Volmer and Tafel reactions, with Tafel corresponding to the rate-determining step.

Supplementary Materials: The following supporting information can be downloaded at: <https://www.mdpi.com/article/10.3390/catal13010022/s1>. Figure S1: Comparison of the diffraction parameters of the TiO_2 /C material and of the TiC JCPDS and of the anatase and rutile phases of titanium oxide; Figure S2: Diffraction parameters of M/C and C materials; Figure S3: Adjustment of the Ti 2p spectra for TiO_2 /C, 1% Pt/ TiO_2 /C and 1% Ag/ TiO_2 /C catalysts; Figure S4: HR-TEM images obtained for 1% Pt/C (left) and 1% Ag/C (right); Figure S5: Cyclic voltammetry curves for M/ TiO_2 /C and M/C catalysts in 0.5 M H_2SO_4 at 50 mV s^{-1} ; Figure S6: Electric equivalent circuit (EEC) model proposed by Armstrong and Henderson; Figure S7: Adjustment of impedance spectroscopy of Ag/ TiO_2 /C.

Author Contributions: Conceptualization, F.B.O. and E.A.T.; methodology, F.B.O.; software, F.B.O., P.H.; validation, F.B.O. and E.A.T.; formal analysis, F.B.O., V.A.P. and P.H.; investigation, F.B.O., V.A.P. and P.H.; resources, V.A.P., P.H. and E.A.T.; data curation, F.B.O., V.A.P. and P.H.; writing—original draft preparation, F.B.O., V.A.P., P.H. and E.A.T.; writing—review and editing, F.B.O., V.A.P. and E.A.T.; visualization, F.B.O., V.A.P., P.H. and E.A.T.; supervision, E.A.T.; project administration, E.A.T.; funding acquisition, E.A.T. All authors have read and agreed to the published version of the manuscript.

Funding: This research was funded by São Paulo State Research Foundation (FAPESP—grant number 2019/22183-6) provided financial support. FBO is thankful to Conselho Nacional de Desenvolvimento Científico e Tecnológico for the scholarship (CNPq—grant number: 150072/2019-8).

Data Availability Statement: Not applicable.

Conflicts of Interest: The authors declare that they have no known competing financial interest or personal relationship that could have appeared to influence the work reported in this paper.

References

1. Strmcnik, D.; Lopes, P.P.; Genorio, B.; Stamenkovic, V.R.; Markovic, N.M. Design principles for hydrogen evolution reaction catalyst materials. *Nano Energy* **2016**, *29*, 29–36. [[CrossRef](#)]
2. Zeng, M.; Li, Y. Recent advances in heterogeneous electrocatalysts for the hydrogen evolution reaction. *J. Mater. Chem. A* **2015**, *3*, 14942–14962. [[CrossRef](#)]
3. Yan, Y.; Xia, B.Y.; Zhao, B.; Wang, X. A review on noble-metal-free bifunctional heterogeneous catalysts for overall electrochemical water splitting. *J. Mater. Chem. A* **2016**, *4*, 17587–17603. [[CrossRef](#)]
4. Fang, S.; Zhu, X.; Liu, X.; Gu, J.; Liu, W.; Wang, D.; Yao, T. Uncovering near-free platinum single-atom dynamics during electrochemical hydrogen evolution reaction. *Nat. Commun.* **2020**, *11*, 1029. [[CrossRef](#)] [[PubMed](#)]
5. Cheng, N.; Stambula, S.; Wang, D.; Banis, M.N.; Liu, J.; Riese, A.; Sun, X. Platinum single-atom and cluster catalysis of the hydrogen evolution reaction. *Nat. Commun.* **2016**, *7*, 13638. [[CrossRef](#)] [[PubMed](#)]
6. Yin, X.P.; Wang, H.J.; Tang, S.F.; Lu, X.L.; Shu, M.; Si, R.; Lu, T.B. Engineering the coordination environment of single-atom platinum anchored on graphdiyne for optimizing electrocatalytic hydrogen evolution. *Angew. Chem. Int. Ed. Engl.* **2018**, *57*, 9382–9386. [[CrossRef](#)]
7. Zeng, Z.; Su, Y.; Quan, X.; Choi, W.; Zhang, G.; Liu, N.; Zhang, S. Single-atom platinum confined by the interlayer nano space of carbon nitride for efficient photocatalytic hydrogen evolution. *Nano Energy* **2020**, *69*, 104409. [[CrossRef](#)]
8. Wang, D.Y.; Gong, M.; Chou, H.L.; Pan, C.J.; Chen, H.A.; Wu, Y.; Wang, Y.L. Highly active and stable hybrid catalyst of cobalt-doped FeS₂ nanosheets–carbon nanotubes for hydrogen evolution reaction. *J. Am. Chem. Soc.* **2015**, *137*, 1587–1592. [[CrossRef](#)]
9. Danilov, F.I.; Tsurkan, A.V.; Vasil'eva, E.A.; Protsenko, V.S. Electrocatalytic activity of composite Fe/TiO₂ electrodeposits for hydrogen evolution reaction in alkaline solutions. *Int. J. Hydrogen Energy* **2016**, *41*, 7363–7372. [[CrossRef](#)]
10. Protsenko, V.S.; Bogdanov, D.A.; Korniy, S.A.; Kityk, A.A.; Baskevich, A.S.; Danilov, F.I. Application of a deep eutectic solvent to prepare nanocrystalline Ni and Ni/TiO₂ coatings as electrocatalysts for the hydrogen evolution reaction. *Int. J. Hydrogen Energy* **2019**, *44*, 24604–24616. [[CrossRef](#)]
11. Kullaiiah, R.E.L.; Hegde, A.C. Effect of TiO₂ nanoparticles on hydrogen evolution reaction activity of Ni coatings. *Int. J. Miner. Metall. Mater.* **2018**, *25*, 472–479. [[CrossRef](#)]
12. Benea, L.; Pavlov, A.I. Ni-TiO₂ nanocomposite coatings as cathode material for hydrogen evolution reaction. *Optoelectron. Adv. Mater. Rapid Commun.* **2013**, *7*, 895–899.
13. Marino, T.; Figoli, A.; Molino, A.; Argurio, P.; Molinari, R. Hydrogen and oxygen evolution in a membrane photoreactor using suspended nanosized Au/TiO₂ and Au/CeO₂. *ChemEngineering* **2019**, *3*, 5. [[CrossRef](#)]
14. Roy, N.; Leung, K.T.; Pradhan, D. Nitrogen doped reduced graphene oxide-based Pt–TiO₂ nanocomposites for enhanced hydrogen evolution. *J. Phys. Chem. C* **2015**, *119*, 19117–19125. [[CrossRef](#)]
15. Wang, Y.; Chen, L.; Yu, X.; Wang, Y.; Zheng, G. Superb Alkaline Hydrogen Evolution and Simultaneous Electricity Generation by Pt-Decorated Ni₃N Nanosheets. *Adv. Energy Mater.* **2017**, *7*, 1601390. [[CrossRef](#)]
16. Bukola, S.; Merzougui, B.; Akinpelu, A.; Zeama, M. Cobalt and nitrogen co-doped tungsten carbide catalyst for oxygen reduction and hydrogen evolution reactions. *Electrochim. Acta* **2016**, *190*, 1113–1123. [[CrossRef](#)]
17. Sasaki, K.; Zhang, L.; Adzic, R.R. Niobium oxide-supported platinum ultra-low amount electrocatalysts for oxygen reduction. *Phys. Chem. Chem. Phys.* **2008**, *10*, 159–167. [[CrossRef](#)]
18. Masuda, T.; Fukumitsu, H.; Fugane, K.; Togasaki, H.; Matsumura, D.; Tamura, K.; Uosaki, K. Role of Cerium Oxide in the Enhancement of Activity for the Oxygen Reduction Reaction at Pt–CeOx Nanocomposite Electrocatalyst -An in Situ Electrochemical X-ray Absorption Fine Structure Study. *J. Phys. Chem. C* **2012**, *116*, 10098–10102. [[CrossRef](#)]
19. Lopes, T.; Kucernak, A.; Malko, D.; Ticianelli, E.A. Mechanistic insights into the oxygen reduction reaction on metal–N–C electrocatalysts under fuel cell conditions. *ChemElectroChem* **2016**, *3*, 1580–1590. [[CrossRef](#)]
20. Do Rêgo, U.A.; Lopes, T.; Bott-Neto, J.L.; Tanaka, A.A.; Ticianelli, E.A. Oxygen reduction electrocatalysis on transition metal–nitrogen modified tungsten carbide nanomaterials. *J. Electroanal. Chem.* **2018**, *810*, 222–231. [[CrossRef](#)]
21. Yu, B.; Jin, J.; Wu, H.; Wang, S.; Xia, Q.; LIU, H. Iron and nickel doped CoSe₂ as efficient non precious metal catalysts for oxygen reduction. *Int. J. Hydrogen Energy* **2017**, *42*, 236–242. [[CrossRef](#)]
22. Du, Y.; Cheng, G.; Luo, W. Colloidal synthesis of urchin-like Fe doped NiSe₂ for efficient oxygen evolution. *Nanoscale* **2017**, *9*, 6821–6825. [[CrossRef](#)] [[PubMed](#)]
23. Wang, L.; Mahoney, E.G.; Zhao, S.; Yang, B.; Chen, J.G. Low loadings of platinum on transition metal carbides for hydrogen oxidation and evolution reactions in alkaline electrolytes. *ChemComm* **2016**, *52*, 3697–3700. [[CrossRef](#)] [[PubMed](#)]
24. Hassan, A.; Paganin, V.A.; Ticianelli, E.A. Pt modified tungsten carbide as anode electrocatalyst for hydrogen oxidation in proton exchange membrane fuel cell: CO tolerance and stability. *Appl. Catal. B* **2015**, *165*, 611–619. [[CrossRef](#)]
25. Gubán, D.; Borbáth, I.; Pászti, Z.; Sajó, I.; Drotár, E.; Hegedűs, M.; Tompos, A. Preparation and characterization of novel Ti_{0.7}W_{0.3}O₂-C composite materials for Pt-based anode electrocatalysts with enhanced CO tolerance. *Appl. Catal. B* **2015**, *174*, 455–470. [[CrossRef](#)]
26. Kim, G.J.; Kwon, D.W.; Hong, S.C. Effect of Pt particle size and valence state on the performance of Pt/TiO₂ catalysts for CO oxidation at room temperature. *J. Phys. Chem. C* **2016**, *120*, 17996–18004. [[CrossRef](#)]

27. Tauster, S.J.; Fung, S.C.; Baker, R.T.K.; Horsley, J.A. Strong interactions in supported-metal catalysts. *Science* **1981**, *211*, 1121–1125. [[CrossRef](#)] [[PubMed](#)]
28. Ometto, F.B.; Carbonio, E.A.; Teixeira-Neto, É.; Villullas, H.M. Changes induced by transition metal oxides in Pt nanoparticles unveil the effects of electronic properties on oxygen reduction activity. *J. Mater. Chem. A* **2019**, *7*, 2075–2086. [[CrossRef](#)]
29. Bruix, A.; Rodriguez, J.A.; Ramirez, P.J.; Senanayake, S.D.; Evans, J.; Park, J.B.; Illas, F. New Type of Strong Metal–Support Interaction and the Production of H₂ through the Transformation of Water on Pt/CeO₂ (111) and Pt/CeO_x/TiO₂ (110) Catalysts. *J. Am. Chem. Soc.* **2012**, *134*, 8968–8974. [[CrossRef](#)]
30. Pan, Y.; Wen, M. Noble metals enhanced catalytic activity of anatase TiO₂ for hydrogen evolution reaction. *Int. J. Hydrogen Energy* **2018**, *43*, 22055–22063. [[CrossRef](#)]
31. Kim, J.H.; Chang, S.; Kim, Y.T. Compressive strain as the main origin of enhanced oxygen reduction reaction activity for Pt electrocatalysts on chromium-doped titania support. *Appl. Catal. B* **2014**, *158*, 112–118. [[CrossRef](#)]
32. Timperman, L.; Lewera, A.; Vogel, W.; Alonso-Vante, N. Nanostructured platinum becomes alloyed at oxide-composite substrate. *Electrochem. Commun.* **2010**, *12*, 1772–1775. [[CrossRef](#)]
33. Jiao, Y.; Zheng, Y.; Jaroniec, M.; Qiao, S.Z. Design of electrocatalysts for oxygen-and hydrogen-involving energy conversion reactions. *Chem. Soc. Rev.* **2015**, *44*, 2060–2086. [[CrossRef](#)] [[PubMed](#)]
34. Ono, L.K.; Croy, J.R.; Heinrich, H.; Cuenya, B.R. Oxygen chemisorption, formation, and thermal stability of Pt oxides on Pt nanoparticles supported on SiO₂/Si(001): Size effects. *J. Phys. Chem. C* **2011**, *115*, 16856–16866. [[CrossRef](#)]
35. Agnihotri, S.; Mukherji, S.; Mukherji, S. Immobilized silver nanoparticles enhance contact killing and show highest efficacy: Elucidation of the mechanism of bactericidal action of silver. *Nanoscale* **2013**, *5*, 7328–7340. [[CrossRef](#)] [[PubMed](#)]
36. Erraria, A.M.; Carapeto, A.P.; Rego, D.; Botelho, A.M. X-ray photoelectron spectroscopy: Silver salts revisited. *Vacuum* **2012**, *86*, 1988–1991. [[CrossRef](#)]
37. Godoi, D.R.M.; Villullas, H.M.; Zhu, F.-C.; Jiang, Y.-X.; Sun, S.-G.; Guo, J.; Sun, L.; Chen, R. A comparative investigation of metal-support interactions on the catalytic activity of Pt nanoparticles for ethanol oxidation in alkaline medium. *J. Power Sources* **2016**, *311*, 81–90. [[CrossRef](#)]
38. Lewera, A.; Timperman, L.; Roguska, A.; Alonso-Vante, N. Metal-support interactions between nanosized Pt and metal oxides (WO₃ and TiO₂) studied using X-ray photoelectron spectroscopy. *J. Phys. Chem. C* **2011**, *115*, 20153–20159. [[CrossRef](#)]
39. Camacho, B.R.; Morais, C.; Valenzuela, M.A.; Alonso-Vante, N. Enhancing oxygen reduction reaction activity and stability of platinum via oxide-carbon composites. *Catalysts* **2013**, *202*, 36–43. [[CrossRef](#)]
40. Kim, J.H.; Kwon, G.; Lim, H.; Zhu, C.; You, H.; Kim, Y.T. Effects of transition metal doping in Pt/M-TiO₂ (M = V, Cr, and Nb) on oxygen reduction reaction activity. *J. Power Sources* **2016**, *320*, 188–195. [[CrossRef](#)]
41. Bard, A.J.; Faulkner, L.R. Fundamentals and applications. *Electrochem. Methods* **2001**, *2*, 580–632.
42. Bockris, J.O.; Reddy, A.K.N.; Gamboa-Aldeco, M.E. *Modern Electrochemistry*; Plenum Press: New York, NY, USA, 1998.
43. Erdey-Grúz, T.; Volmer, M. Zur Theorie der Wasserstoff Überspannung Zeitschrift für Physikalische Chemie. *Z. Für Phys. Chem.* **1930**, *150A*, 203–213. [[CrossRef](#)]
44. Heyrovský, J. A theory of overpotential. *Recueil des Travaux Chimiques des Pays-Bas* **1927**, *46*, 582–585. [[CrossRef](#)]
45. Tafel, J. Über die Polarisation bei kathodischer Wasserstoffentwicklung. *Z. Für Phys. Chem.* **1905**, *50U*, 641–712. [[CrossRef](#)]
46. Du, H.; Kong, R.M.; Guo, X.; Qu, F.; Li, J. Recent progress in transition metal phosphides with enhanced electrocatalysis for hydrogen evolution. *Nanoscale* **2018**, *10*, 21617–21624. [[CrossRef](#)] [[PubMed](#)]
47. Masa, J.; Batchelor-Mcauley, C.; Schuhmann, W.; Compton, R.G. Koutecky-Levich analysis applied to nanoparticle modified rotating disk electrodes: Electrocatalysis or misinterpretation? *Nano Res.* **2014**, *7*, 71–78. [[CrossRef](#)]
48. Armstrong, R.D.; Henderson, M. Impedance plane display of a reaction with an adsorbed intermediate. *J. Electroanal. Chem.* **1972**, *39*, 81–90. [[CrossRef](#)]
49. Navarro-Flores, E.; Chong, Z.; Omanovic, S. Characterization of Ni, NiMo, NiW and NiFe electroactive coatings as electrocatalysts for hydrogen evolution in an acidic medium. *J. Mol. Catal. A Chem.* **2005**, *226*, 179–197. [[CrossRef](#)]
50. Šimpraga, R.; Tremiliosi-Filho, G.; Qian, S.Y.; Conway, B.E. In situ determination of the ‘real area factor’ in H₂ evolution Electrocatalysis at porous Ni-Fe composite electrodes. *J. Electroanal. Chem.* **1997**, *424*, 141–151. [[CrossRef](#)]
51. Castro, E.B.; de Giz, M.J.; Gonzalez, E.R.; Vilche, J.R. An electrochemical impedance study on the kinetics and mechanism of the hydrogen evolution reaction on nickel molybdenite electrodes. *Electrochim. Acta* **1997**, *42*, 951–959. [[CrossRef](#)]
52. Xiong, L.; Manthiram, A. Nanostructured Pt-M/C (M = Fe and Co) catalysts prepared by microemulsion method for oxygen reduction in proton exchange membrane fuel cells. *Electrochim. Acta* **2005**, *50*, 2323–2329. [[CrossRef](#)]
53. Santos, L.G.R.A.; Oliveira, C.H.F.; Moraes, I.R.; Ticianelli, E.A. Oxygen reduction reaction in acid medium on Pt-Ni/C prepared by microemulsion method. *J. Electroanal. Chem.* **2006**, *596*, 141–148. [[CrossRef](#)]
54. Kumar, P.; Mittal, K.L. *Handbook of Microemulsion Science and Technology*; Marcel Dekker: New York, NY, USA, 1999.
55. Capek, I. Preparation of metal nanoparticles in water-in-oil (w/o) microemulsions. *Adv. Colloid Interface Sci.* **2004**, *110*, 49–74. [[CrossRef](#)]
56. Briggs, D.; Seah, M.P. *Practical Surface Analysis, Auger and X-Ray Photoelectron Spectroscopy*; John Wiley & Sons: Chichester, UK, 1990; Volume 1.
57. Smith, G.C. *Surface Analysis by Electron Spectroscopy*; Plenum: New York, NY, USA, 1994.

58. Scofield, J. Hrn. Hartree-Slater subshell photoionization cross-sections at 1254 and 1487 eV. *J. Electron Spectrosc. Relat. Phenom.* **1976**, *8*, 129–137. [[CrossRef](#)]
59. Chastain, J.; King, J.R.; Roger, C. Handbook of X-ray photoelectron spectroscopy. *Perkin-Elmer Corp.* **1992**, *40*, 221.
60. Naumkin, A.V.; Kraut-Vass, A.; Gaarenstroom, S.W.; Powell, C.J. NIST X-ray Photoelectron Spectroscopy Database. NIST Standard Reference Database 20, v. 4.1. Available online: <http://srdata.nist.gov/XPS/> (accessed on 7 April 2021).

Disclaimer/Publisher’s Note: The statements, opinions and data contained in all publications are solely those of the individual author(s) and contributor(s) and not of MDPI and/or the editor(s). MDPI and/or the editor(s) disclaim responsibility for any injury to people or property resulting from any ideas, methods, instructions or products referred to in the content.